RSC Advances

PAPER

View Article Online
View Journal | View Issue

Cite this: *RSC Adv.*, 2024, **14**, 17814

Coating effect of renatured triple-helix lentinan on the morphology and antimicrobial activity of ZnO synthesized by hydrothermal method

Xuewei Jia,[a] Yihong Wu,[a] Zhiyang Liu,[a] Yuxiang Dai,[a] Tianxiao Li,[a] Mingqi Gao*[b] and Chunping Xu *[a]

Received 1st March 2024
Accepted 23rd May 2024

DOI: 10.1039/d4ra01590h

rsc.li/rsc-advances

Polysaccharides are considered to be ideal green raw materials for enhancing biocompatibility and dispersion effects of nanoparticles. In this study, we coated and dispersed ZnO nanoparticles (NPs) using the denaturation–renaturation process of a triple helix glucan lentinan (LNT), induced by changes in pH value within the reaction system. Various ZnO/LNT composites with different particle sizes and crystal morphologies were prepared and characterized. The results demonstrated that renatured LNT (r-LNT) effectively encapsulated the {10$\bar{1}$0} crystal planes of ZnO, preventing crystal growth during the renaturation process and resulting in smaller, uniformly dispersed nanoparticles. Among the samples, ZnO/r-LNT-2 exhibited significantly higher antimicrobial activity, and it had a certain inhibitory effect on various plant pathogens. It also displayed the highest inhibitory effect against *Candida albicans*, with a minimum inhibitory concentration (MIC) of up to 8 μg mL^{-1}. Consistently, ZnO/r-LNT-2 generated the highest amount of reactive oxygen species (ROS), thus exhibiting the most effective antimicrobial activity. However, excessive introduction of the dispersant LNT may reduce these activities. This study provides a foundation for further exploring the detailed mechanism of ROS generation catalyzed by ZnO and for harnessing the full potential of this type of antimicrobial agent.

1. Introduction

In recent years, nanomaterials have found extensive applications in bioengineering, particularly nano-zinc oxide materials (ZnO NPs), due to their unique properties of low cytotoxicity, excellent broad-spectrum antimicrobial properties, and resistance prevention against bacteria.[1–3] The biocidal effects of ZnO result from their ability to generate reactive oxygen species, which significantly impede the growth and reproduction of microorganisms.[4,5] Alternatively, they can interact with the surface of microorganisms or achieve cell internalization in the form of ZnO or Zn^{2+}, resulting in the destruction of the cell membrane, the leakage of its contents, and the death of the cells.[6] Notably, the toxic mechanisms of ZnO NPs with different morphologies and structures are also different.[7] The existence form of zinc (ZnO or Zn^{2+}) may vary depending on the composition of the medium and the physical and chemical properties of the nanoparticles, such as particle size, morphology, surface modification, and dispersibility.[8,9] To enhance the antimicrobial activity of ZnO NPs, recent research has focused on effectively modifying their properties using biocompatible and economical materials.

Polysaccharides possess abundant availability, non-toxicity, biodegradability, and excellent biocompatibility, making them ideal materials for dispersing nanoparticles.[10–12] The hydroxyl groups present in polysaccharides facilitate bonding formation with various materials, such as metals, DNA, and proteins.[13–15] This allows stable dispersion of nanoparticles while greatly improving their biocompatibility. Lentinan (LNT), a triple helix polysaccharide, can denature into a single-chain conformation under high temperature, strong alkali, or other polar solvents. Upon temperature decrease, pH value reduction, or removal of the hydroxyl group destruction caused by the polar solvent, LNT can renature into a helical conformation. Previous studies have shown that the denaturation–renaturation process of LNT exhibits strong affinity with guests, including gold nanoparticles, selenium nanoparticles, and gold-silver nanoalloys, leading to effective dispersion.[16–18]

In the study of crystal growth habits, controlling crystal morphology is a desired outcome. Different application fields require crystal materials with varied morphologies, making the preparation of crystals with specific morphologies significant for growth theory studies. Reaction temperature, time, and dispersing agent in the solution can influence the crystallization speed, crystal size, and microscopic morphology of ZnO crystal nucleus-related crystal faces, thereby controlling the

[a]*Zhengzhou University of Light Industry, Zhengzhou, Henan, China. E-mail: c.p.xu@zzuli.edu.cn; Tel: +86 371 86609637*

[b]*China Tobacco Henan Industrial Co., Ltd., Zhengzhou, Henan, China. E-mail: gaomq1984@126.com; Tel: +86 371 61291027*

growth of crystal materials with specific morphologies.[19–21] In this work, ZnO NPs were prepared by hydrothermal method with NaOH and zinc acetate. ZnO NPs were coated and dispersed by the denaturation–renaturation process of LNT induced by changes in pH value in the reaction system. A series of ZnO/LNT composites were subsequently prepared and characterized. The effects of reaction temperature, polysaccharide conformation change and concentration on the morphology of ZnO NPs were investigated. Additionally, antimicrobial activities of the nanocomposites were tested.

2. Materials and methods

2.1. Materials

Zinc acetate dihydrate ($Zn(CH_3COO)_2 \cdot 2H_2O$), sodium hydroxide (NaOH), terephthalate and *N*-acetyl-L-cysteine (NAC) were analytically pure and purchased from Shanghai Aladdin, China. 2′,7′-Dichlorofluorescein-diacetate (DCFH-DA, ≥97%) and phosphate buffered saline (PBS, pH = 7.4) were purchased from Sigma, Germany. Triple-helical glucan lentinan (t-LNT) was isolated from the fruiting bodies of *Lentinus edodes*. The detailed procedures have been previously reported.[22] Deionized water (>18 MΩ) was utilized in all experiments.

2.2. Synthesis of ZnO/LNT

t-LNT was dissolved in a 1 M NaOH solution for half an hour to break the intra- and intermolecular hydrogen bonds, resulting in a single-chain t-LNT (coded as s-LNT) which was used in subsequent experiments. ZnO/r-LNT nanocomposites of various compositions were synthesized by fixing the final zinc acetate and s-LNT concentration (as listed in Table 1). As shown in Fig. 1, s-LNT solution was slowly added to the zinc acetate solution at 25 °C and the pH was adjusted to 9 with NaOH. The mixture was stirred at 90 °C for 4 h to obtain ZnO nanoparticles. As the pH value dropped below 10, s-LNT could renature into the triple-helix polysaccharide r-LNT.[15] After completion of the hydrothermal reaction, the mixture was subsequently dialyzed against deionized water for two days using a 4 L beaker and a cellulose tube with an M_w cutoff of 8000. The water was replaced every 8 h. The dialyzed mixture was freeze-dried to obtain a series of ZnO/r-LNT samples. As a control, ZnO NPs (ZnO) were directly synthesized in the absence of LNT. ZnO/r-LNT-110 was synthesized at a higher reaction temperature of 110 °C. For ZnO/t-LNT synthesis, t-LNT was dissolved in deionized water without alkali treatment and applied to the synthesized ZnO/t-LNT. ZnO, ZnO/t-LNT, and ZnO/r-LNT-110 were also obtained after dialysis and freeze-drying.

2.3. Characterization of ZnO/LNT

The particle size distribution of ZnO and ZnO/LNTs was determined using a static light scattering (SLS) analyzer (Microtrac S3500, USA) at 25 °C. The crystal structure and phase purity of ZnO and ZnO/LNTs were analyzed using an X-ray diffractometer (XRD, D8-Advance, Bruker, Germany). The patterns were recorded over a range of 2θ from 5 to 70°. The morphology and microstructure of ZnO and ZnO/LNTs were examined using a high-resolution cold field emission scanning electron microscope operated at a voltage of 3 kV (Regulus 8100, Hitachi, Japan). Fourier transform infrared spectra (FTIR) spectroscopic analysis were recorded on a Nicolet spectrometer (Nicolet iS50, Thermo Nicolet Co., USA) in a range from 400 cm^{-1} to 4000 cm^{-1}. X-ray photoelectron spectroscopy (XPS) spectra were detected on a Thermo Scientific K-Alpha spectrometer (USA).

2.4. Determination of MIC

Three plant pathogenic bacteria, *Erwinia carotovora*, *Pseudomonas syringae*, and *Ralstonia solanacearum*, were collected by our laboratory and used in this study. *Bacillus subtilis* (ATCC6051), *Pseudomonas aeruginosa* (ATCC27853) and *Candida albicans* (SC5314) were obtained from the American Type Culture Collection (ATCC). The antimicrobial activities of LNT, ZnO and ZnO/LNTs were investigated against three plant pathogenic bacteria and three model strains using a liquid growth inhibition assay. Five strains of bacteria were adjusted to 10^6 CFU mL^{-1} in LB medium (Solarbio, China), while *C. albicans* was adjusted to 10^5 CFU mL^{-1} in RPMI 1640 medium (Solarbio, China). Then, LNT, ZnO and ZnO/LNTs were added to each test tube to achieve final concentrations of 0, 2, 4, 8, 16, 32, 64, 128, 256, and 512 μg mL^{-1}. The cultures were incubated at 30 °C 24 h, and growth inhibition was determined by measuring the optical densities at 540 nm (OD540s) using a microplate reader (Model 550, Bio-Rad, China). The experiments were performed in triplicate.

2.5. Antimicrobial mechanism

In the dissolution experiment of zinc ions, suspensions of ZnO and ZnO/LNTs with a ZnO concentration of 2 mg mL^{-1} in RPMI

Table 1 The final zinc acetate and LNT concentration required for the synthesis of different ZnO/LNTs and ZnO, pH value of reaction system and dispersion of products

Sample code	$Zn(CH_3COO)_2 \cdot 2H_2O$ conc. (mg mL^{-1})	LNT conc. (mg mL^{-1})	T (°C)	Final pH value	Crystallinity (%)	Crystallite size (nm)	Dispersion
ZnO	8.8	0	90	9	80.1	41.1	Precipitate
ZnO/t-LNT	8.8	2.0	90	9	77.1	38.9	Precipitate
ZnO/r-LNT-110	8.8	2.0	110	9	79.2	41.0	Precipitate
ZnO/r-LNT-1	8.8	1.0	90	9	67.8	23.9	Well-dispersed
ZnO/r-LNT-2	8.8	2.0	90	9	61.3	23.2	Well-dispersed
ZnO/r-LNT-3	8.8	10	90	9	57.5	21.5	Well-dispersed

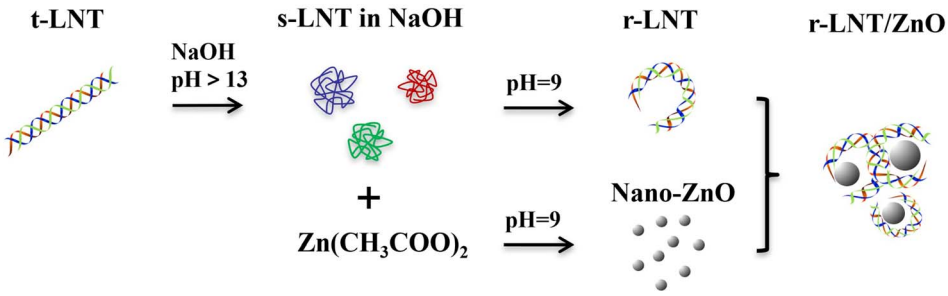

Fig. 1 Scheme of ZnO NPs dispersion by r-LNT.

1640 medium were prepared and then incubated at 30 °C for 4–12 h. After centrifugation, the supernatant was filtered with a 0.44 μm filter membrane. The corresponding medium was used as blank controls. The dissolution of Zn^{2+} was detected by inductively coupled plasma mass spectrometry (ICP-MS, Elan 9000, PerkinElmer, USA).

The ˙OH produced by ZnO NPs and ZnO/LNTs can react with terephthalate, and the product is 2-hydroxyterephthalic acid ester with fluorescent activity.[4] The reaction product is very stable for several hours, and the fluorescence intensity at 425 nm can be used to quantitatively detect the ˙OH concentration. Different sample suspensions with a ZnO concentration of 2 mg mL^{-1} and the same volume of terephthalate solution with a concentration of 4 mM were mixed by magnetic stirring at room temperature for 10 min and then left at room temperature for different times. The reactions were stopped by removing the ZnO particles from the suspensions through centrifuging and filtering with Millipore membrane. The fluorescence intensity of the filtrate containing 2-hydroxyterephthalate at 425 nm was detected by a fluorescence spectrophotometer (F-7000, Hitachi, Japan).

H_2O_2 produced by ZnO and ZnO/LNTs were determined using a hydrogen peroxide detection kit (Beyotime Biotechnology, China). Different sample suspensions with ZnO concentrations of 2 mg mL^{-1} were prepared. Then the ZnO particles in the suspension were removed after standing for 12 h at room temperature. According to the kit instructions, 50 μL of the sample was added to the detection hole, and 100 μL of hydrogen peroxide detection reagent was added to each hole, then gently oscillated and mixed, and placed at room temperature for 30 min. A_{560} was then measured and the concentration of H_2O_2 in the samples was calculated from the standard curve.

Intracellular ROS accumulation was evaluated by DCF fluorescence assay. *C. albicans* was adjusted to 10^5 CFU mL^{-1} in RPMI 1640 medium and pre-cultured in 24-well plates for 24 h to form biofilms. The biofilms were then treated with different concentrations of ZnO/r-LNT-2 for 12 h. The culture medium was removed and 300 μL of diluted DCFH-DA (10 μM) was added. The cells were incubated in the dark for 20 min and washed three times with RPMI medium to remove DCFH-DA. An appropriate amount of PBS solution was added, and images were taken with a fluorescence microscope (NI-E, Nikon, Japan).

3. Results and discussion

3.1. Formation of ZnO

ZnO and ZnO/LNT nanocomposites were synthesized by hydrothermal reaction. As the reaction progressed, precipitation was observed at the bottom of the ZnO, ZnO/t-LNT, and ZnO/r-LNT-110 solution. Fig. 2 depicts the particle size distribution of ZnO and ZnO/LNT nanocomposites in water. Due to the poor dispersion of ZnO, ZnO/t-LNT and ZnO/r-LNT-110 in water, the particle size of all samples was detected immediately after ultrasonic pre-dispersion. It can be observed that the addition of polysaccharides greatly reduces the particle size of ZnO. The particle size of ZnO, ZnO/t-LNT, and ZnO/r-LNT-110 is on a micron scale. The ZnO/r-LNT composites coated with polysaccharides, after denaturation and renaturation at 90 °C, exhibited good monodispersity. The average diameters of ZnO/r-LNT-1, ZnO/r-LNT-2, and ZnO/r-LNT-3 were measured to be 431 nm, 296 nm, and 241 nm, respectively. The average particle size of the nanocomposites decreased with increasing amounts of polysaccharides added. This indicates that polysaccharides can effectively prevent the growth of ZnO crystals during the renaturation process, leading to the formation of smaller and uniformly dispersed nanoparticles.

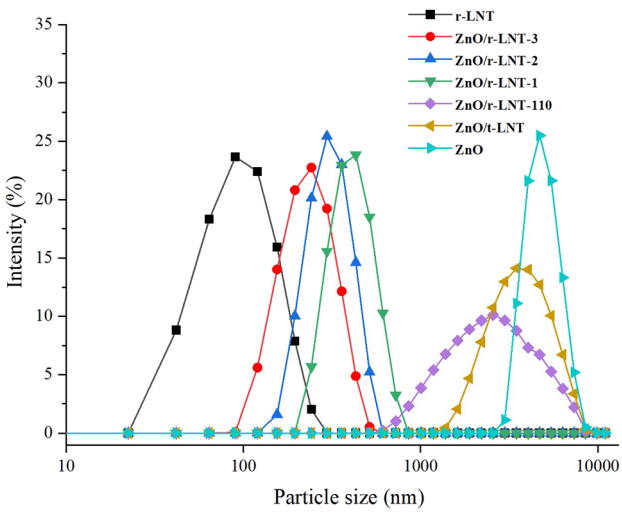

Fig. 2 Size distribution of ZnO, LNT and their nanocomposites in aqueous solution.

The XRD profiles of LNT, ZnO and different ZnO/LNT are shown in Fig. 3. The lentinan used in this work is an amorphous natural macromolecule extracted from the fruiting body. There is no typical fingerprint, and its XRD spectrum shows a slightly inclined curve. ZnO exhibited strong diffraction peaks at 2θ = 31.7°, 34.4°, 36.2°, 47.5°, 56.6°, 62.9°, 66.4°, 68.0° and 69.1°, which correspond to (100), (002), (101), (102), (110), (103), (200), (112) and (201) crystal plane characteristic peaks of ZnO hexagonal wurtzite structure (JCPDS card no. 36-1451). The XRD patterns of different ZnO/LNT samples showed similar peaks to that of ZnO. With an increase in LNT content, the XRD pattern of the sample exhibited a similar inclined trend to that of LNT, but still maintained the corresponding crystal diffraction peak of ZnO. This confirms the successful synthesis of ZnO/LNT nanocomposites. Moreover, there were no diffraction peaks corresponding to impurities such as Zn or $Zn(OH)_2$, indicating the high purity level of the samples.[23] The addition of LNT resulted in peak broadening and reduced intensity, which may be attributed to the smaller crystallite size and decreased crystallinity.[7,24] The average crystallite size was calculated using the Scherer formula (eqn (1)), and the crystallinity was calculated through the integration method using eqn (2).[25] The results were list in Table 1. Which concluded that the crystallinity of the ZnO/r-LNT-1, ZnO/r-LNT-2, and ZnO/r-LNT-3 were lower than ZnO, ZnO/t-LNT, and ZnO/r-LNT-110, which confirmed the adsorption of renatured LNT chains (under 90 °C) on the surface of ZnO nanoparticles reduces their crystallinity and crystallite size. Additionally, the changes in the intensity of the (100) and (002) peaks also indicate modifications in the crystal morphology of ZnO with the addition of different LNTs. The crystal morphology of ZnO and Zn/r-LNT-110 differs from that of other samples.

$$\text{Crystallinity}\% = \frac{\text{area under crystalline peaks}}{\text{area under all peaks}} \times 100\% \quad (1)$$

$$D = \frac{k\lambda}{\beta \cos\theta} \quad (2)$$

In the equation, D stands for the crystallite size (nm), k for the form factor (0.89), λ for the wavelength of the CuK_α radiation, β for FWHM for a specific peak, and θ for the Bragg's angle of diffraction.

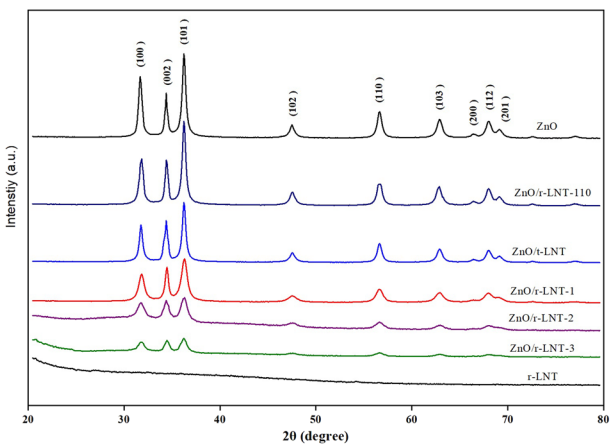

Fig. 3 XRD spectra of ZnO, LNT and their nanocomposites.

Fig. 4 depicts SEM images of ZnO and five ZnO/LNT nanocomposites. SEM images of pure ZnO synthesized at 90 °C (Fig. 4A) show near-spherical particles with clear boundaries, with an average particle size of about 4.8 μm (counting 100 particles). The particles are gathered by lamellae and form a flower-like structure, with a lamellae thickness of about 30 nm. ZnO/t-LNT exhibits a fusiform flower structure, and the spindle length is about 200 nm. In the synthesis of ZnO/r-LNT-110, the growth speed of ZnO crystal is faster at 110 °C. The ZnO nanoparticles appear needle-like and aggregate to form sea urchin-like particles, with a needle length of about 1.0 μm and a diameter of about 20 nm. At a reaction temperature of 90 °C, ZnO can be coated with r-LNT to obtain a series of uniformly dispersed nanoparticles with smaller particle sizes. Fig. 4D–F show that with increasing amounts of s-LNT added, the nanoflowers gradually disappear, and the ZnO nanoparticles tend to become spherical particles. This is consistent with the observations made during the synthesis process and the particle size distribution results obtained using an SLS analyzer.

FTIR spectra of ZnO, LNT, ZnO/r-LNT-1, ZnO/r-LNT-2, and ZnO/r-LNT-3 are presented in Fig. 5. The peaks observed at 3440, 3389 cm^{-1} corresponding to OH group stretching vibrations of ZnO and LNT samples. The peaks at 2930 cm^{-1}, 1640 cm^{-1} and 1030–1300 cm^{-1} are common absorption peaks of polysaccharides. ZnO exhibits the vibrational peak at 468 cm^{-1} which attributed to the stretching vibration mode of Zn–O bond.[7] While increasing the concentration of r-LNT, the band shifts to lower wavenumber which presumed the bonding between the hydroxyl groups of chitosan and ZnO. In addition, the Zn–O stretching band also observed in ZnO/r-LNT.

XPS spectra of ZnO and ZnO/r-LNTs are depicted in Fig. 6. Obvious characteristic peaks such as C 1s, O 1s and Zn 2p can be observed in the survey spectra.[4] The characteristic peak of Na 1s appears in the spectrum of ZnO, which should be caused by the adsorption of a small amount of CH_3COONa on the surface. The binding energy in the XPS spectrum makes. C 1s spectra mainly show the presence of both C–C (284.5 eV), C–O (286.0 eV) and C=O (287.8) species in the surface of the materials. These carbons species are consistent with the presence of C-containing functional groups of polysaccharides or CH_3COONa on the surface. Fig. 6 also shows the spectra of O 1s, confirming the presence of oxygen in the surface associated with C–O bonds. In the case of the Zn 2p spectra, two interesting peaks were found. The peak at 1020.6 eV, and 1021.3 eV corresponds to Zn $2p_{3/2}$ of ZnO and ZnO/r-LNT, with the second peak at much higher binding energies corresponding to Zn $2p_{1/2}$. The peak distance between these two peaks is a signature of the presence of ZnO nanoparticles, in good agreement with XRD data. It can be clearly seen that the adsorption of polysaccharides on the surface of ZnO resulted in a lower binding energy shift of Zn 2p and O 1s of ZnO/r-LNT.

3.2. Formation mechanism of the ZnO/r-LNT

The reformation of dissociated triple helices of LNT generally depends on the environmental conditions. Many of the

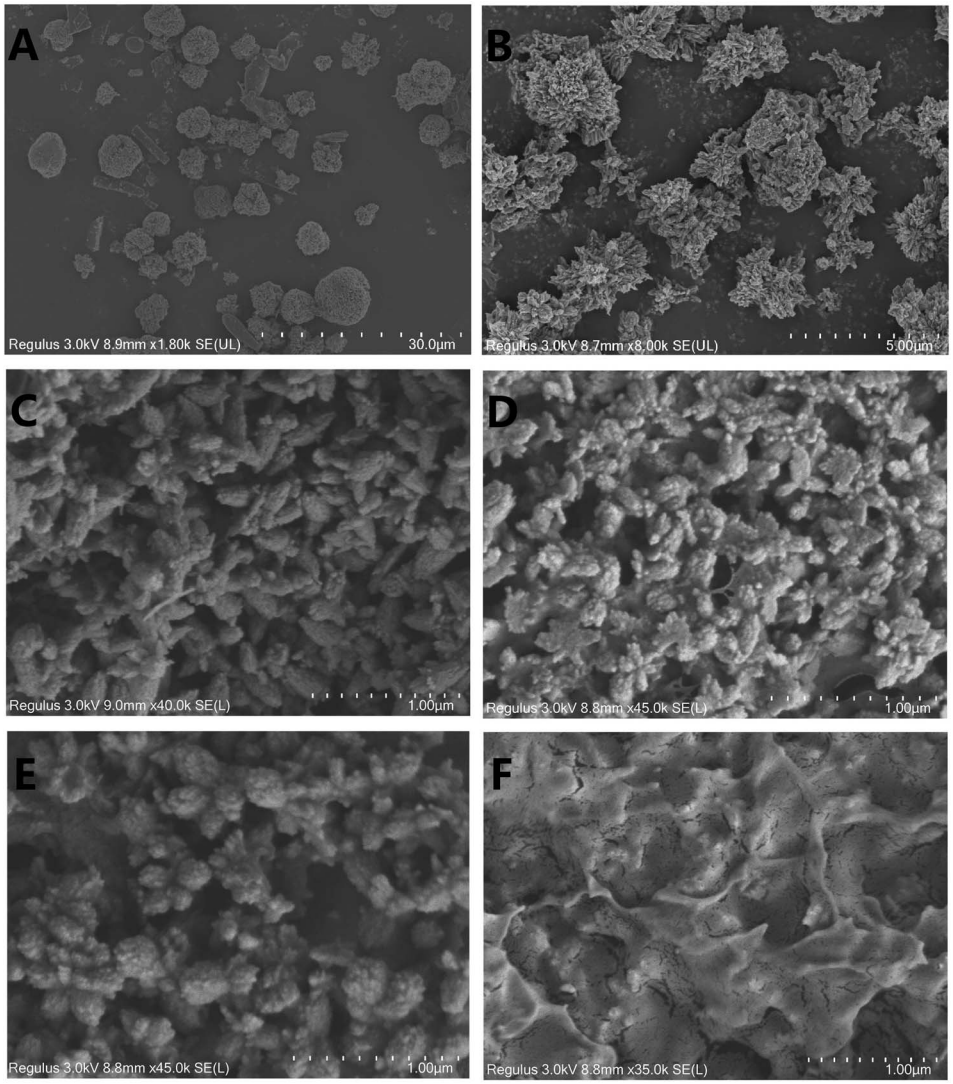

Fig. 4 SEM images of ZnO (A), ZnO/r-LNT-110 (B), ZnO/t-LNT (C), ZnO/r-LNT-1 (D), ZnO/r-LNT-2 (E) and ZnO/r-LNT-3 (F).

renatured s-LNT chains appear as macrocycles with diameters up to tens of nanometers at 90 °C, while, most of them become linear triple-helix polysaccharides at 110 °C. Similar structural changes were observed in the reformation of scleroglucan after annealing at different temperatures by Brant *et al.*[26] Based on the above data, a preliminary mechanism was proposed to describe the synthesis and dispersion of ZnO/r-LNT.

In the lower-temperature reaction system without polysaccharide addition. ZnO self-assembles into a lamellar structure along the non-*c*-axis [10$\bar{1}$0] direction and eventually forms a large-size lamellar aggregated flower-like structure.[27,28] At the same temperature, the rigid polysaccharide chains of t-LNT provide crystal attachment growth points, increasing the number of crystal seeds. Additionally, the coating effect of polysaccharide chains on the crystal surface inhibits further growth along the non-*c*-axis direction, resulting in the formation of a short cone aggregation flower structure with slightly smaller particle size.[29] At high temperature, a large number of ZnO crystal nuclei were formed in the solution, and the diffusion rate of zinc ions was also fast, leading to preferential rapid growth along the [0001] crystal orientation. The renaturation of the polysaccharide chain is slow, and adopt a random coil or linear structure, and the coating effect on zinc oxide is poor. Similarly, ZnO/r-LNT-110 with larger particles was also generated.

In the synthesis process of ZnO/r-LNT-90, LNT was initially destroyed by NaOH into a single-chain s-LNT. After adding zinc acetate, the pH value of the solution decreased to 9, allowing for renaturation into a triple helix structure, appearing as macrocycles with diameters up to tens of nanometers. The {10$\bar{1}$0} crystal plane family of ZnO crystals is non-polar.[30,31] Cyclic r-LNT can encapsulate the {10$\bar{1}$0} crystal planes through hydrogen bonds and hydrophobic interactions, further inhibiting crystal growth and resulting in spherical ZnO nanoparticles with smaller particle sizes.[15,32] This is consistent with the results of the XRD pattern. In the three ZnO/r-LNT-90 samples, an increase in polysaccharide content leads to a decrease in crystallinity and crystallite size.

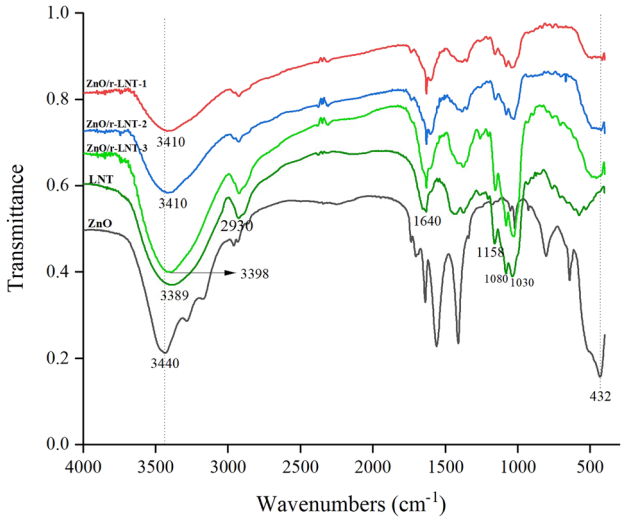

Fig. 5 FTIR spectra of ZnO, LNT, ZnO/r-LNT-1, ZnO/r-LNT-2, and ZnO/r-LNT-3.

3.3. Antimicrobial activities of ZnO/r-LNT

The minimum inhibitory concentrations (MICs) of different ZnO nanoparticles against five bacteria and *Candida albicans*, determined by liquid medium, are shown in Table 2. There are differences in the inhibitory effects of ZnO nanoparticles on different strains. This may due to the different cell wall structures, metabolic pathways, and resistance mechanisms of different strains.[33] It can be observed that different ZnO nanoparticles have varying inhibitory effects on microorganisms. ZnO/r-LNT-2 exhibits significantly higher antimicrobial activity compared to other samples. Generally, smaller nanoparticle sizes correlate with higher biological activity. However, ZnO/r-LNT-3, despite having the highest polysaccharide content and the best dispersion effect on ZnO, exhibits poor antimicrobial activity.

In general, within a certain range (particle size above 5 nm), the antimicrobial effect increases as particle size decreases. However, ZnO nanoparticles with small particle sizes tend to agglomerate and are difficult to disperse, which greatly limits their application performance. The antimicrobial activity mechanism of ZnO nanoparticles is currently considered to have three main possibilities: (1) the release of Zn^{2+} ions; (2) excessive ROS, such as superoxide anion ($^{\bullet}O_2^-$), hydroxyl radical ($^{\bullet}OH$) and hydrogen peroxide (H_2O_2), which caused oxidative damage to different cells; (3) other non-oxidative.[33,34] In this work, the antimicrobial activity of ZnO with different particle sizes and crystal forms will be further explored by taking *Candida albicans* as an example due to its pronounced inhibitory effect.

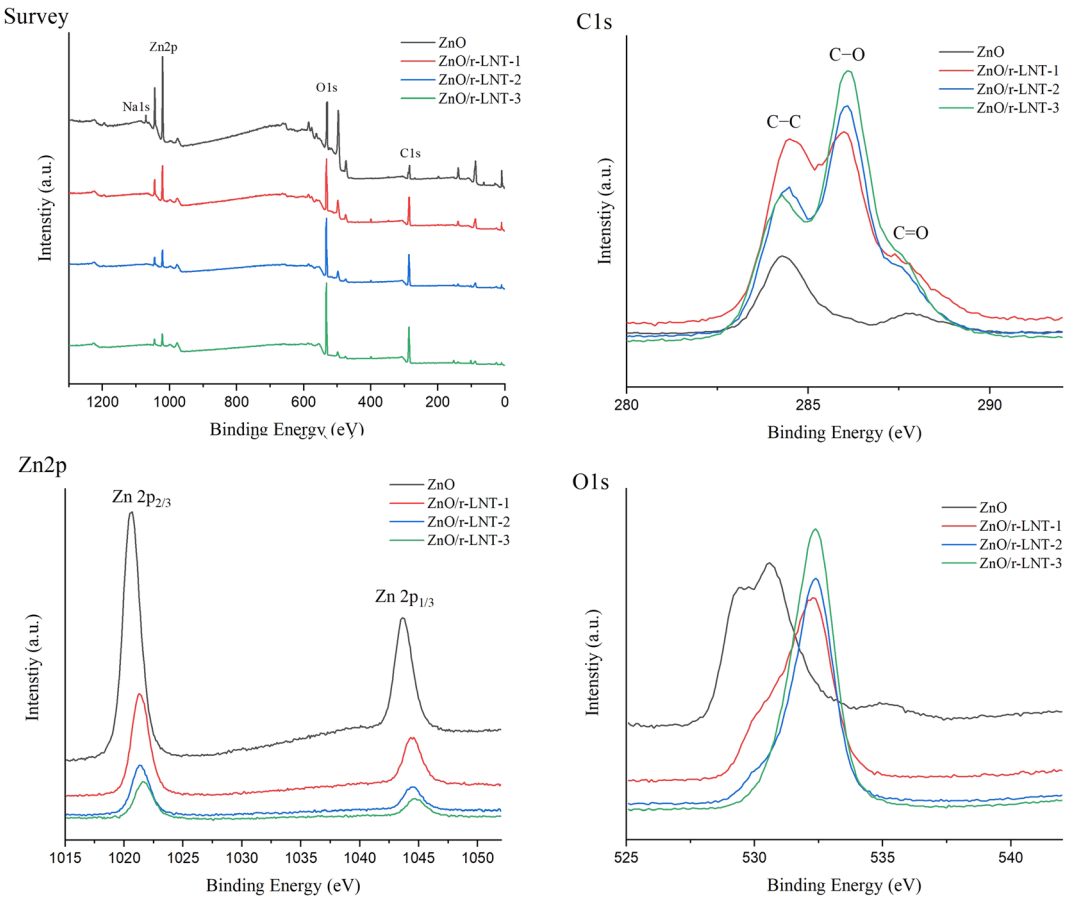

Fig. 6 XPS spectra of ZnO, ZnO/r-LNT-1, ZnO/r-LNT-2 and ZnO/r-LNT-3.

Table 2 The antimicrobial activity of different ZnO/LNTs and ZnO against three plant pathogens and three standard strains

	MIC (μg mL^{-1})						
Strains	ZnO	ZnO/r-LNT110	ZnO/t-LNT	ZnO/r-LNT-1	ZnO/r-LNT-2	ZnO/r-LNT-3	LNT
Pseudomonas syringae	128	128	128	64	64	128	—
Erwinia carotovora	256	256	32	32	16	32	—
Ralstonia solanacearum	256	128	128	32	8	64	—
Bacillus subtilis	256	128	64	64	16	128	—
Pseudomonas aeruginosa	256	128	128	128	64	128	—
Candida albicans	128	128	128	16	8	32	—

ICP-MS measurements of Zn^{2+} released of different ZnO NPs in the RPMI 1640 medium are summarized in Table 3. It can be seen that concentrations of zinc released were similar, indicating that Zn^{2+} release should not be the main reason for the inhibition of *Candida albicans*. While ZnO/r-LNT-3 with the smallest particle size can dissolve zinc ions faster, the concentration of dissolved zinc ions after 12 h is essentially the same as that of other samples.

The concentrations of two common reactive oxygen species, namely ˙OH and H_2O_2, were further detected. As shown in Fig. 7, the cumulative concentration of ˙OH increases with time, indicating that different ZnO nanoparticles can continuously catalyze the production of ˙OH. However, due to the instability of the free radical active substance itself, it slowly degrades. With the increase of time, the growth rate of ˙OH slowed down, and the curve flattened between 4–12 h. Generally, ZnO/r-LNTs can produce more ˙OH compared to ZnO with larger particle sizes. ZnO/r-LNT-2 exhibits the fastest ˙OH production rate, reaching maximum concentration in approximately 4 h, while ZnO/r-LNT-3 shows a relatively slow rate of ˙OH production, with the curve flattening around 8–12 h, but it is still higher than that of ZnO.

As shown in Fig. 8, the results of H_2O_2 were similar to those of ˙OH. After 12 h of incubation, ZnO/r-LNT-2 exhibits the strongest ability to produce H_2O_2, with a concentration of 19.8 μg mL^{-1}. Combined these results with the antimicrobial activity of different ZnO nanoparticles against *Candida albicans*, it indicated that the dissolution of Zn^{2+} is not the main mechanism determining the antimicrobial activity of ZnO, whereas the production of different reactive oxygen species is the primary antimicrobial mechanism. However, according to numerous literature reports, polysaccharides have some antioxidant activity.[35,36] The zinc oxide in the ZnO/r-LNT-3, which has the best dispersion effect and the smallest particle size,

Table 3 Analysis of released Zn^{2+} in RPMI 1640 media from different ZnO/LNTs and ZnO

	Conc. of Zn^{2+} in RPMI 1640 (μg mL^{-1})	
Sample	4 h	12 h
ZnO	6.54	7.99
ZnO/r-LNT-110	6.81	7.88
ZnO/t-LNT	6.92	8.12
ZnO/r-LNT-1	7.14	8.32
ZnO/r-LNT-2	7.26	8.66
ZnO/r-LNT-3	8.19	8.54

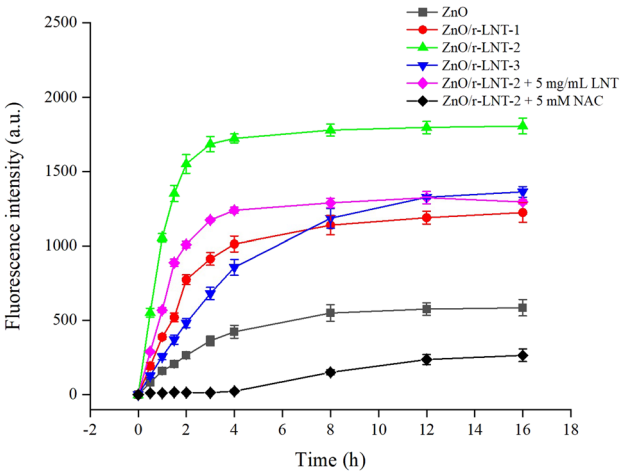

Fig. 7 Production of ˙OH in ZnO, ZnO/r-LNT-1, ZnO/r-LNT-2, ZnO/r-LNT-3, and ZnO/r-LNT-2 + 5 mg mL^{-1} LNT suspensions at different times measured by fluorescence method. All sample contains 2 mg mL^{-1} ZnO.

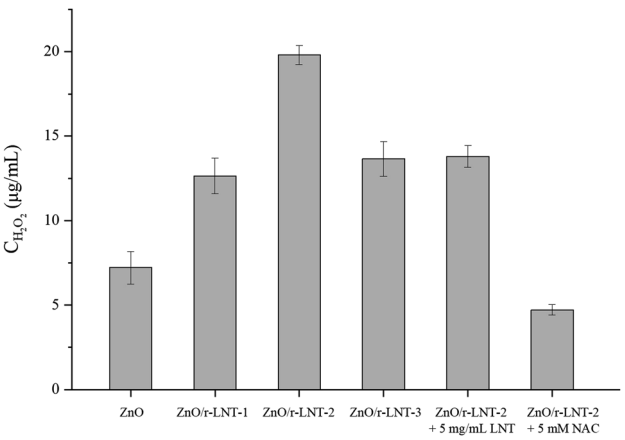

Fig. 8 H_2O_2 produced by ZnO, ZnO/r-LNT-1, ZnO/r-LNT-2, ZnO/r-LNT-3, and ZnO/r-LNT-2 + 5 mg mL^{-1} LNT suspensions. All sample contains 2 mg mL^{-1} ZnO. All particles in the suspension were removed after standing for 12 h at room temperature.

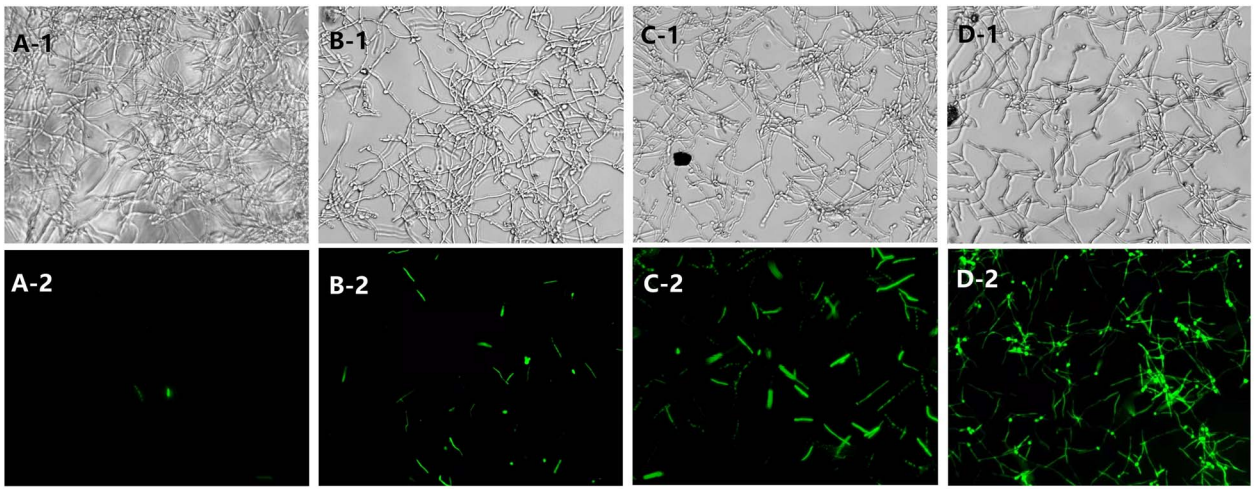

Fig. 9 Intracellular ROS accumulation of *C. albicans* mature biofilms after incubation with 0 (A1 and A2), 8 (B1 and B2), 16 (C1 and C2), 32 μg mL^{-1} (D1 and D2) ZnO in composite ZnO/r-LNT-2 *via* fluorescence microscope observation.

produces not the most reactive oxygen species. This may be due to the fact that the antioxidant activity of the polysaccharide itself slows down the accumulation of reactive oxygen species in the solution. Additionally, excessive coating of polysaccharides may also impact the production of reactive oxygen species. For comparison, 5 mg mL^{-1} LNT or 5 mM NAC was added to ZnO/r-LNT-2, and the generation of $^{\bullet}OH$ and H_2O_2 was measured using the same method. NAC is a commonly used antioxidant that has the effect of inhibiting oxidative stress.[37] It can be observed that the polysaccharide has a NAC-like function, and its addition leads to a reduction in ROS, but the antioxidant capacity is weak.

Finally, ZnO/r-LNT-2, which exhibits the best inhibitory effect, was used to investigate its effect on the intracellular level of reactive oxygen species in *Candida albicans*. The results are shown in Fig. 9, where Fig. 9A1–D1 represent *Candida albicans* treated with 0 μg mL^{-1}, 4 μg mL^{-1}, 16 μg mL^{-1}, and 64 μg mL^{-1} ZnO/r-LNT-2, respectively, under an ordinary light microscope field of view. Corresponding fluorescence microscope images under the same field of view are shown in Fig. 9A2–D2. It can be observed that as the concentration of ZnO/r-LNT-2 increases, the density of mycelium in the biofilm continuously decreases, and the level of reactive oxygen species in the mycelium significantly increases. Under the treatment group of 64 μg mL^{-1} ZnO/r-LNT-2, the level of reactive oxygen species in almost all mycelium exceeds the normal value. Prolonged peroxidation of cells leads to damage in various membrane structures, including enzyme activities, thereby achieving antimicrobial activity. These results indicate that ZnO/r-LNT-2 can inhibit *Candida albicans* by inducing the accumulation of intracellular reactive oxygen species.

4. Conclusion

ZnO nanoparticles were prepared through hydrothermal synthesis, employing LNT as a dispersant to systematically investigate the influence of LNT concentration and conformational alterations on the dispersive behavior. Additionally, the inhibitory potency and antimicrobial mechanisms of various ZnO/LNT composites against diverse microbial strains were delved into. The results demonstrated that ZnO/r-LNT, which was dispersed through the LNT denaturation–renaturation process, exhibited better dispersive properties, absent of precipitation and nanoparticle aggregation. Notably, ZnO/r-LNT-2 displayed significantly augmented antimicrobial activity in comparison to other samples. Furthermore, it exhibited the utmost inhibitory effect against *Candida albicans*, with a MIC value of 8 μg mL^{-1}. The antimicrobial mechanism study revealed that the antimicrobial activity of ZnO was primarily attributed to the generation of ROS, rather than Zn^{2+} dissolution.

Author contributions

Xuewei Jia: conceptualization, methodology, writing – original draft. Yihong Wu: investigation, writing – original draft. Zhiyang Liu: investigation. Yuxiang Dai: methodology. Tianxiao Li: methodology. Mingqi Gao: conceptualization, writing – review & editing. Chunping Xu: methodology, writing – review & editing.

Conflicts of interest

The authors declare that they have no known competing financial interests or personal relationships that could have appeared to influence the work reported in this paper.

Acknowledgements

This work was supported by the Henan Provincial Department of Science and Technology Research Project (232102320292) and Major Public Welfare Projects in Henan Province (201300110200).

References

1 B. Jana, A. Chatterjee, D. Roy, S. Ghorai, D. Pan, S. K. Pramanik, N. Chakraborty and J. Ganguly, Chitosan/benzyloxy-benzaldehyde modified ZnO nano template having optimized and distinct antiviral potency to human cytomegalovirus, *Carbohydr. Polym.*, 2022, **2781**, 18965–118965.

2 A. H. Bashal, S. M. Riyadh, W. Alharbi, K. H. Alharbi, T. A. Farghaly and K. D. Khalil, Bio-based (Chitosan-ZnO) nanocomposite: synthesis, characterization, and its use as recyclable, ecofriendly biocatalyst for synthesis of thiazoles tethered azo groups, *Polymers*, 2022, **14**(3), 386.

3 A. Tanwar, P. Date and D. Ottoor, ZnO NPs incorporated gelatin grafted polyacrylamide hydrogel nanocomposite for controlled release of ciprofloxacin, *Colloids Interface Sci. Commun.*, 2021, **42**, 100413.

4 X. Xu, D. Chen, Z. Yi, M. Jiang, L. Wang, Z. Zhou, X. Fan, Y. Wang and D. Hui, Antimicrobial mechanism based on H_2O_2 generation at oxygen vacancies in ZnO crystals, *Langmuir*, 2013, **29**(18), 5573–5580.

5 J. Liu, Y. Wang, J. Ma, Y. Peng and A. Wang, A review on bidirectional analogies between the photocatalysis and antibacterial properties of ZnO, *J. Alloys Compd.*, 2019, **783**, 898–918.

6 S. H. S. Dananjaya, R. S. Kumar, M. Yang, C. Nikapitiya, J. Lee and M. De Zoysa, Synthesis, characterization of ZnO-chitosan nanocomposites and evaluation of its antifungal activity against pathogenic Candida albicans, *Int. J. Biol. Macromol.*, 2018, **108**, 1281–1288.

7 A. Dhanalakshmi, A. Palanimurugan and B. Natarajan, Efficacy of saccharides bio-template on structural, morphological, optical and antibacterial property of ZnO nanoparticles, *Mater. Sci. Eng., C*, 2018, **90**, 95–103.

8 S. G. Kang, K. E. Lee, M. Singh and R. Vinayagam, Salicylic-zinc nanocomposites with enhanced antibacterial activity, *Coatings*, 2023, **13**(5), 941.

9 H. A. Rudayni, N. A. Alenazi, A. M. Rabie, M. Aladwani, L. M. Alneghery, G. M. Abu-Taweel, A. A. Allam and M. R. Abukhadra, Biological characterization of microwave based synthesized ZnO and Ce doped ZnO nanoflowers impeded chitosan matrix with enhanced antioxidant and anti-diabetic properties, *Int. J. Biol. Macromol.*, 2023, **242**, 124713.

10 J. Estrada-Urbina, A. Cruz-Alonso, M. Santander-Gonzalez, A. Mendez-Albores and A. Vazquez-Duran, Nanoscale zinc oxide particles for improving the physiological and sanitary quality of a Mexican landrace of red maize, *Nanomaterials*, 2018, **8**(4), 247.

11 J. Cheng and H. Wang, Construction and application of nano ZnO/eugenol@yam starch/microcrystalline cellulose active antibacterial film, *Int. J. Biol. Macromol.*, 2023, **239**, 124215.

12 Y. Zhang, C. Chen, J. Wang and L. Zhang, Polysaccharide-based polyelectrolytes hollow microcapsules constructed by layer-by-layer technique, *Carbohydr. Polym.*, 2013, **96**, 528–535.

13 A. Ebrahiminezhad, F. Moeeni, S. M. Taghizadeh, M. Seifan, C. Bautista, D. Novin, Y. Ghasemi and A. Berenjian, Xanthan gum capped ZnO microstars as a promising dietary zinc supplementation, *Foods*, 2019, **8**(3), 88.

14 C. Xu, M. Ojeda, R. A. D. Arancon, A. A. Romero, J. L. Domingo, M. Gómez, J. Blanco and R. Luque, Bioinspired porous ZnO nanomaterials from fungal polysaccharides: advanced materials with unprecedented low toxicityin vitrofor human cells, *ACS Sustainable Chem. Eng.*, 2015, **3**, 2716–2725.

15 Y. Zhang, S. Li, X. Wang, L. Zhang and P. C. K. Cheung, Advances in lentinan: Isolation, structure, chain conformation and bioactivities, *Food Hydrocolloids*, 2011, **25**, 196–206.

16 X. Jia, Q. Liu, S. Zou, X. Xu and L. Zhang, Construction of selenium nanoparticles/β-glucan composites for enhancement of the antitumor activity, *Carbohydr. Polym.*, 2015, **117**, 434–442.

17 X. Jia, Y. Yao, G. Yu, L. Qu, T. Li, Z. Li and C. Xu, Synthesis of gold-silver nanoalloys under microwave-assisted irradiation by deposition of silver on gold nanoclusters/triple helix glucan and antifungal activity, *Carbohydr. Polym.*, 2020, **238**, 116169.

18 X. Jia, X. Xu and L. Zhang, Synthesis and stabilization of gold nanoparticles induced by denaturation and renaturation of triple helical β-glucan in water, *Biomacromolecules*, 2013, **14**, 1787–1794.

19 Y.-J. Pu, N. Morishita, T. Chiba, S. Ohisa, M. Igarashi, A. Masuhara and J. Kido, Efficient electron injection by size- and shape-controlled zinc oxide nanoparticles in organic light-emitting devices, *ACS Appl. Mater. Interfaces*, 2015, **7**, 25373–25377.

20 S. Raha and M. Ahmaruzzaman, ZnO nanostructured materials and their potential applications: progress, challenges and perspectives, *Nanoscale Adv.*, 2022, **4**, 1868–1925.

21 R. S. Rai, J. P. Girish, V. Bajpai, M. I. Khan, N. Elboughdiri, A. Shanableh and R. Luque, An eco-friendly approach on green synthesis, bio-engineering applications, and future outlook of ZnO nanomaterial: a critical review, *Environ. Res.*, 2023, **221**, 114807.

22 L. Zhang, X. Zhang, Q. Zhou, P. Zhang, M. Zhang and X. Li, Triple helix of β-d-glucan from Lentinus edodes in 0.5 M NaCl aqueous solution characterized by light scattering, *Polym. J.*, 2001, **33**, 317–321.

23 S. T. Lin, M. Thirumavalavan, T. Y. Jiang and J. F. Lee, Synthesis of ZnO/Zn nano photocatalyst using modified polysaccharides for photodegradation of dyes, *Carbohydr. Polym.*, 2014, **105**, 1–9.

24 G. Magesh, G. Bhoopathi, N. Nithya, A. P. Arun and E. Ranjith Kumar, Structural, morphological, optical and biological properties of pure ZnO and agar/zinc oxide nanocomposites, *Int. J. Biol. Macromol.*, 2018, **117**, 959–966.

25 S. R. Mishra, V. Gadore, R. Verma, K. R. B. Singh, J. Singh and M. Ahmaruzzaman, In2S3 incorporated into

CO32−@Ni/Fe/Zn trimetallic LDH as a bi-functional novel nanomaterial for enzymatic urea sensing and removal of sulfur-containing pharmaceutical from aqueous streams, *Chem. Eng. J.*, 2023, **475**, 146207.

26 T. M. McIntire and D. A. Brant, Imaging of individual biopolymers and supramolecular assemblies using noncontact atomic force microscopy, *Biopolymers*, 1997, **42**, 133–146.

27 B. Li and Y. Wang, Facile synthesis and enhanced photocatalytic performance of flower-like ZnO hierarchical microstructures, *J. Phys. Chem. C*, 2010, **114**, 890–896.

28 L. Miao, B. Shi, N. Stanislaw, C. Mu and K. Qi, Facile synthesis of hierarchical ZnO microstructures with enhanced photocatalytic activity, *Mater. Sci.-Pol.*, 2017, **35**, 45–49.

29 G.-X. Tong, F.-F. Du, Y. Liang, Q. Hu, R.-N. Wu, J.-G. Guan and X. Hu, Polymorphous ZnO complex architectures: selective synthesis, mechanism, surface area and Zn-polar plane-codetermining antibacterial activity, *J. Mater. Chem. B*, 2013, **1**, 454–463.

30 C. Wang, Y. Gao, L. Wang and P. Li, Morphology regulation, structural, and photocatalytic properties of ZnO hierarchical microstructures synthesized by a simple hydrothermal method, *Phys. Status Solidi A*, 2017, **214**, 1600876.

31 X. Xu, H. Pang, Z. Zhou, X. Fan, S. Hu and Y. Wang, Preparation of multi-interfacial ZnO particles and their growth mechanism, *Adv. Powder Technol.*, 2011, **22**, 634–638.

32 G. Magesh, G. Bhoopathi, N. Nithya, A. P. Arun and E. R. Kumar, Tuning effect of polysaccharide chitosan on structural, morphological, optical and photoluminescence properties of ZnO nanoparticles, *Superlattices Microstruct.*, 2018, **117**, 36–45.

33 H. Kotrange, A. Najda, A. Bains, R. Gruszecki, P. Chawla and M. M. Tosif, Metal and metal oxide nanoparticle as a novel antibiotic carrier for the direct delivery of antibiotics, *Int. J. Mol. Sci.*, 2021, **22**, 9596.

34 T. Hassanein, A. Mohammed, W. Mohamed, R. Sobh and M. Zahran, Optimized synthesis of biopolymer-based zinc oxide nanoparticles and evaluation of their antibacterial activity, *Egypt. J. Chem.*, 2021, **64**(7), 3767–3790.

35 M. J. Meng, R. Huo, Y. Wang, N. A. Ma, X. L. Shi, X. Z. Shen and G. J. Chang, Lentinan inhibits oxidative stress and alleviates LPS-induced inflammation and apoptosis of BMECs by activating the Nrf2 signaling pathway, *Int. J. Biol. Macromol.*, 2022, **222**, 2375–2391.

36 X. Ji, J. Guo, F. Pan, F. Kuang, H. Chen, X. Guo and Y. Liu, Structural elucidation and antioxidant activities of a neutral polysaccharide from Arecanut (Areca catechu L.), *Front. Nutr.*, 2022, **9**, 853115.

37 Z. Chen, J. Shi, Y. Zhang, S. Han, J. Zhang and G. Jia, DNA oxidative damage as a sensitive genetic endpoint to detect the genotoxicity induced by titanium dioxide nanoparticles, *Nanomaterials*, 2022, **12**(15), 2616.